

The following publication Wang, H., Sun, Y., He, W., Zhou, Y., Lee, S. C., & Dong, F. (2018). Visible light induced electron transfer from a semiconductor to an insulator enables efficient photocatalytic activity on insulator-based heterojunctions. *Nanoscale*, 10(33), 15513-15520 is available at <https://doi.org/10.1039/C8NR03845G>.



Nanoscale

ARTICLE

Visible light induced electrons transfer from semiconductor to insulator enables efficient photocatalytic activity on insulator-based heterojunctions

Received 00th January 20xx,
Accepted 00th January 20xx

DOI: 10.1039/x0xx00000x

www.rsc.org/

Hong Wang^a, Yanjuan Sun^a, Wenjie He^a, Ying Zhou^b, Shun Cheng Lee^c, Fan Dong^{*a,b}

Abstract: Photogenerated electrons play a vital role in photocatalysis as they could induce the formation of radicals participating in the reaction or recombine with holes preventing them from the subsequent redox reaction. In this work, we explore the earth-abundant insulator coupled with semiconductor and construct insulator-semiconductor heterojunctions to effectively realize the efficient electrons transfer from semiconductor to insulator and thus the enhanced charge carriers separation on semiconductor. This result will challenge the traditional opinion that free electrons cannot be transferred onto insulator. Taking the BaCO₃ insulator as a case study, the combined experimental and theoretical evidences indicate that the photogenerated electrons from the semiconductor BiOI could transfer directly to BaCO₃ insulator through a preformed electron delivery channel when they are coupled to form BaCO₃/BiOI heterojunctions. The potential difference between the Bi layer of BiOI (5.03 eV) and carbonate layer of BaCO₃ (12.37 eV) would drive the excited electrons from Bi atoms transfer cross the energy barrier to the adjacent carbonate layer under the visible light irradiation. Consequently, the free electrons on BaCO₃ can be utilized to produce the oxidative radicals ($\cdot\text{OH}$, $\cdot\text{O}_2^-$ and $^1\text{O}_2$) participating in the photocatalytic oxidation reaction. The *in situ* FT-IR spectra illustrate that the visible light induced active species in the heterojunctions could react with NO, making it being firstly oxidized to high valence state intermediates (NO^+ and NO_2^+) and then converted to the final product of nitrates. This research offers new perspectives to explore insulator-based photocatalyst and unravel the gas-phase photocatalytic reaction mechanism.

1. Introduction

Photocatalysis as a great technology can be driven directly by sunlight irradiation and has been widely applied for environmental remediation.¹⁻³ The photocatalysis efficiency is mainly governed by the following three aspects: (1) the light absorption ability of the photocatalyst; (2) the separation and transfer rate of photogenerated carriers; (3) the photocatalytic redox reaction

efficiency.⁴ Although the narrow band-gap semiconductors possess high visible light absorption ability (such as, BiOI and AgI), they display low photocatalytic activity due to the fast charge recombination, which greatly hampers their practical application in pollution purification.^{5, 6} Convincingly, the efficient charge separation and transfer is the key to enable high photocatalytic efficiency.⁷⁻⁹ In the past few decades, many strategies have been developed, such as doping, surface modification, formation of heterojunctions and metal deposition.¹⁰⁻¹² And the most widely used one is to develop heterojunctions because they could synchronously maintain the light absorption ability and prevent the recombination of charge carriers.^{5, 13, 14}

The earth-abundant insulators with low cost, ease of preparation, good stability and environmental friendly features are widely used in places that can be exposed in sunlight, such as coating, building material and so on.¹⁵ These features are suitable for the photocatalysts in the practical application by fully utilizing the sunlight. Unfortunately, the insulators still suffer from a tremendous barrier in photocatalysis because their band gaps are nearly double compared with that of normal semiconductors as that the free electrons can be hardly excited under light irradiation.¹⁶

Recently, several literatures reported that the insulator could act as a role to block the electrons recombination in solar cells or turn into an efficient ionic conductor by transferring abundant ionic onto the interface of insulator.^{17, 18} In view of this observation, it is acceptable to assume that the insulator can act as a superior

^a Chongqing Key Laboratory of Catalysis and New Environmental Materials, College of Environment and Resources, Chongqing Technology and Business University, Chongqing 400067, China.

^b The Center of New Energy Materials and Technology, School of Materials Science and Engineering, Southwest Petroleum University, Chengdu 610500, China.

^c Department of Civil and Environmental Engineering, The Hong Kong Polytechnic University, Hong Kong, China.

Email: dfctbu@126.com

Electronic Supplementary Information (ESI) available: *In situ* FT-IR measurements (Fig. S1). Schematic diagram of the *in-situ* FT-IR apparatus (Fig. S2). XRD (a) and XPS-survey spectra (b) (Fig. S3). SEM images of pure BaCO₃ and BiOI (Fig. S4). SEM image of Ba-B-3 (a-b), Ba-B-4 (c-d) and Ba-B-5 (e-f) and EDX elemental mapping of Ba (g), C (h), O (i), Bi (j) and I (k) in Ba-B-4 (Fig. S5). UV-vis diffuse reflectance spectra of BiOI, BaCO₃, the physical mixture of BiOI and BaCO₃ (Ba-B-M) (Fig. S6). The electrostatic potentials for (a) BiOI (001), (b) BaCO₃ (002) (Fig. S7). Mott-Schottky curves of (a) BaCO₃ and (b) BiOI (Fig. S8). The nanosecond-level time-resolved fluorescence spectra surveyed at room temperature (Fig. S9). N₂ adsorption-desorption isotherms (a) and the corresponding pore-size distribution curves (b) (Fig. S10). Assignments of the FT-IR bands observed during adsorption processes (Table S1). The SBET and pore size for BaCO₃, BiOI, Ba-B-3, Ba-B-4 and Ba-B-5 (Table S2). Assignments of the FT-IR bands observed during photocatalytic NO oxidation processes (Table S3). See DOI: 10.1039/x0xx00000x

photocatalyst over semiconductor via the transfer of photogenerated electrons from semiconductor to insulator in order to inhibit the charge carriers recombination on semiconductor. In this sense, the insulator's ability to accept the electrons from semiconductor is the key to achieve potential application of insulators in photocatalysis. However, exploring the interfacial charge separation and achieving electrons transfer from semiconductor to insulator are still great challenges.

In this work, we construct the insulator-semiconductor heterojunction via conjugation of BaCO_3 (n-type) with BiOI (p-type) by using a simple precipitation method. The established BaCO_3 - BiOI insulator-semiconductor heterojunctions possess a wide range of visible light absorption, which is beneficial for the production of photogenerated carriers. The combining experimental and theoretical evidences indicate that the electrons delivery channel is preformed between BiOI and BaCO_3 because of a partial overlap of outermost orbitals of the Bi atom in BiOI and O atom in BaCO_3 in the z-direction. Besides, the valance band potential of BiOI is higher than that of BaCO_3 . This potential difference would drive the photogenerated electrons transfer from BiOI to BaCO_3 and thus reduce the accumulation of photogenerated carriers on BiOI , resulting in the prevention of electrons/holes recombination on semiconductor. It is significant to reveal that the free electrons on the insulator could be captured by O_2 and induce the production of abundant active radicals to participate in photocatalysis and thus dramatically boost the photocatalytic performance. The *in situ* FT-IR technology is employed to dynamically monitor the photocatalytic NO oxidation process over the insulator-semiconductor heterojunction. The photocatalytic NO oxidation mechanism is unraveled on the BaCO_3 - BiOI heterojunction. It is found that the produced active radicals could firstly oxide NO adsorption species to high valence state intermedium (NO^+ and NO_2^+) to prevent the accumulation of toxic intermediates. This could enhance the conversion of NO to the final product of nitrates under visible light irradiation. The present work may open up a new area in utilization of the earth-abundant insulators in visible light photocatalysis.

2. Experiment and calculation

2.1 Catalysts preparation

All chemicals are of analytical grade and are used without further treatment. The photocatalysts were prepared by a simple precipitation method. The BaCO_3 (Sigma-Aldrich) was added to 100 mL $\text{Bi}(\text{NO}_3)_3 \cdot 5\text{H}_2\text{O}$ (Sigma-Aldrich) solution (90 mL deionized water and 10 mL glycol) and was stirred for 30 min. Then, the KI solution (30 mL) was added dropwise. The suspension was further stirred for 2 h and aged for 1 h. The final products were collected and watered for three times and dried at 60 °C for 12 h. The molar ratio of $\text{Bi}(\text{NO}_3)_3 \cdot 5\text{H}_2\text{O}$ and KI were controlled at 1:1. The molar ratio of BaCO_3 and BiOI was controlled at 6:3, 6:4, and 6:5, respectively. The samples were labeled as Ba-B-X (X = 3, 4, 5). For comparison, pure BiOI was prepared via the same process without the addition of BaCO_3 .

2.2 Characterization methods

The crystal structure of the samples was recorded using a powder X-ray diffractometer with Cu K α radiation (Model D/Max RA, Rigaku Co, Japan). X-ray photoelectron spectroscopy with an Al K α X-ray radiation source (Thermo ESCALAB 250, USA) was utilized to analyze the chemical composition of the samples. A UV-vis diffuse spectrophotometer was utilized to analyze the optical properties of the samples with 100% BaSO_4 as a reference (UV2550, Shimadzu, Japan). The photoelectrochemical measurements were recorded by an electrochemical system with a three-electrode quartz cell and 0.1 M Na_2SO_4 as the electrolyte (CHI-660B, China). The morphological structure was measured by scanning electron microscopy (SEM, JEOL Model JSM-6490) and transmission electron microscopy (TEM, JEM-2010, Japan). The Brunauer-Emmett-Teller (BET) specific surface area and pore structure measurements were carried out using an ASAP 2020 apparatus. Time-resolved fluorescence decay spectra were gathered using a fluorescence spectrophotometer (Edinburgh Instruments, FLSP-920). Electron spin resonance (ESR) spectra of radicals that were spin-trapped using 5,5-Dimethyl-1-Pyrroline-N-Oxide (DMPO) was employed to verify the formation of superoxide ($\bullet\text{O}_2^-$) and hydroxyl radicals ($\bullet\text{OH}$). 4-oxo-2,2,6,6-Tetramethyl-1-piperidinyloxy (4-oxo-TEMP) was used to detect singlet oxygen, and 2,2,6,6-Tetramethylpiperidine-1-oxyl (TEMPO) was used to characterize photo-generated electrons, respectively.

2.3 Application of insulator-based heterojunction in photocatalytic NOx purification

The photocatalytic performance was evaluated by removing NO (present at ppb levels) from a continuous stream reactor. A UV cut-off filter (420 nm) was applied to remove UV light for the test of photocatalytic activity in visible light region (420–780 nm). The average light intensity was 0.16 $\text{W}\cdot\text{cm}^{-2}$. For this, 0.2 g of the sample was ultrasonically dispersed on two 12-mm diameter glass disks and dried at 60 °C. After natural cooling, the glass disks were placed in the continuous stream reactor. When the NO concentration reached the adsorption-desorption equilibrium, the lamp was turned on. A NO_x analyzer (Thermo Scientific, 42i-TL, USA) recorded the concentrations of NO, NO_2 , and NO_x ($\text{NO} + \text{NO}_2$) every minute. The removal ratio (η) of NO was calculated using η (%) = $(1 - C/C_0) \times 100$ %, where C represents the NO concentration at the outlet of the reactor after turning on the lamp, and C_0 represents the NO concentration when the adsorption-desorption equilibrium is reached before turning on.

2.4 Trapping experiments for visible light induced production of active species

Potassium iodide (KI) was utilized as a hole scavenger, tertbutylalcohol (TBA) was an effective $\bullet\text{OH}$ scavenger, Potassium dichromate ($\text{K}_2\text{Cr}_2\text{O}_7$) was selected as a photo-induced electron scavenger and benzoquinone (BQ) was acted as the $\bullet\text{O}_2^-$ scavenger. Photocatalyst (0.20 g) with different trapping agents was added into 15 mL of H_2O and ultrasonic disperse for 30 min. The aqueous

suspensions were then equally coated onto two glass dishes. Afterwards, the coated dishes were dried at 60 °C in an oven. Ultimately, this two dried dishes were utilized for further photocatalytic NO removal tests.

2.5 Density functional theory calculations

DFT calculations were introduced using the “Vienna *ab initio* simulation package” (VASP5.4) and a generalized gradient correlation function.^{19, 20, 21} A plane-wave basis set with a cut-off energy at 400 eV and the projector-augmented wave method framework was adopted. The Gaussian smearing width was set to 0.2 eV.^{22, 23} The Brillouin zone was sampled with a $3 \times 3 \times 1$ Monkhorst Pack grid. All atoms were allowed to converge to 0.01 eV Å⁻¹. The $15 \times 18 \times 20$ supercell include BiOI with 16 oxygen atoms, 12 bismuth atoms, and 8 iodine atoms, and BaCO₃ with 36 oxygen atoms, 16 barium atoms, and 12 carbon atoms. The supercells of alone BiOI and BaCO₃ were first relaxed, respectively, before the BiOI supercell was placed on the plane of BaCO₃.^{24, 25}

2.6 In situ FT-IR investigation of the photocatalytic NO oxidation process

In situ FT-IR measurements were recorded using a Tensor II FT-IR spectrometer (Bruker), *in situ* reaction bin, gas system, light source, and pretreatment equipment, as shown in Fig. S1. The real-time FT-IR spectrum was used as a background after a heat treatment (110 °C) under high-purity He gas. Then, the reaction gas (50 mL/min NO and 50 mL/min O₂) was sent to the reaction chamber. **Because of the detection sensitivity of *in situ* FT-IR measurement, the concentration of NO (ppb level) is too low to be detected. Therefore, 50 ppm NO is introduced into the reactor for accurate detection of the reaction products.** Under dark conditions, the samples were subjected to 20-min adsorption reactions. Afterwards, the photocatalytic reaction process was carried out for 60 min under visible light irradiation. Finally, the lamp was turned off. The IR spectra were recorded at a given time interval. The scanned area of the infrared spectrum was 4000–600 cm⁻¹. The corresponding schematic diagram was shown in Fig. S2.

3. Results and discussions

3.1 Photoelectrical property and photocatalytic activity

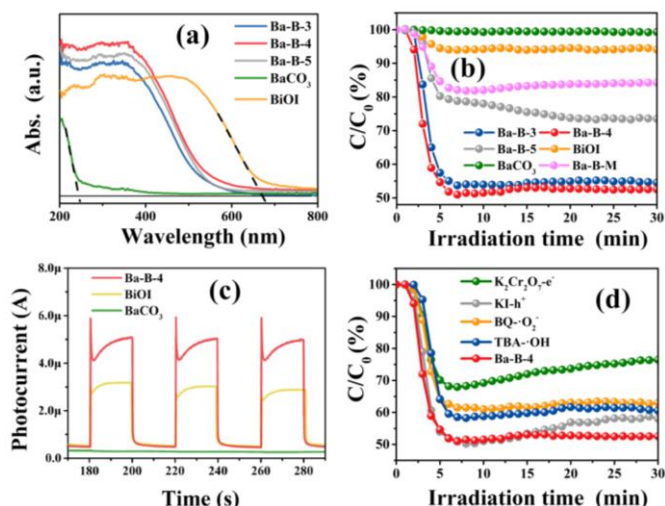


Fig. 1 UV-vis diffuse reflectance spectra (a), Photocatalytic NO purification curves (b), Photocurrent density (c) and Active species trapping (d) for the as-prepared samples.

The prepared samples (Ba-B-X) were characterized by powder XRD (Fig. S3a). The diffraction peaks of prepared pure BiOI (JCPDS 10-0445) and orthorhombic BaCO₃ (JCPDS 01-0506), respectively. For constructed heterojunction, XRD characteristic peaks of both BiOI and BaCO₃ could be observed in the Ba-B-X (X=3, 4, 5), indicating the BiOI-BaCO₃ heterojunctions are comprised. Two pronounced peaks are found in Ba-B-X at 14.7° and 15.8°, which can be indexed to main characteristic peaks of the BiOI, respectively. Besides, the main diffraction peaks at 23.9° of BaCO₃ is detected in the Ba-B-X, demonstrating the heterojunction samples have a two-phase composition: BiOI and BaCO₃. The corresponding XPS spectra for elements (Bi, O, I, Ba and C elements) of BiOI and BaCO₃ are all observed, indicating the successful synthesis of BaCO₃, BiOI and their composites (Fig. S3b). As shown in Fig. S4, the pure BaCO₃ has a rod-like structure and the pure BiOI is assembled by nanosheets. SEM and EDX images (Fig. S5) of Ba-B-X show that the BiOI nanosheets are evenly grown around the surface of BaCO₃, forming a crannied core-shell BaCO₃-BiOI structure. The UV-vis diffuse reflectance spectra (Fig. 1a and S6) reveal that the light absorption region of the insulator-semiconductor heterojunction is extended from 250 nm for BaCO₃ to the around 600 nm, which also indicate that the abundant electrons could be excited under visible light irradiation. The pure BiOI possesses strong visible light absorption ability, but the photocatalytic NO oxidation performance of BiOI is low, which is significantly different from Ba-B-4 with high visible light absorption (Fig. 1b). The Ba-B-4 presents an unprecedented high visible light photocatalytic activity with a NO removal ratio achieving 47.5%, higher than that of typical C-doped TiO₂ (21.8%), Bi₂O₂CO₃ (21.5%) and g-C₃N₄ (32.7%).²⁶⁻²⁸ Besides, these reaction final products accumulated on the photocatalyst surface can be easily removed by water washing and the photocatalyst can be regenerated via this facile method. A simple physical mixture of BaCO₃ and BiOI (Ba-B-M) also exhibits the higher visible light photocatalytic performance (15.9%) than pure BiOI (6%). Note that the photocatalytic NO removal ratio of Ba-B-5 is low compared with Ba-B-3 and Ba-B-4. This is because that the specific surface areas of

Ba-B-5 are significantly reduced (Table S2). As previous reports pointed out that low activity of pure BiOI should arise from the rapid recombination rate of photogenerated carriers.^{5,29}

To illustrate this, the photocurrent density was performed to demonstrate the separation efficiency of photogenerated charge carriers. Fig. 1c shows that the insulator-semiconductor heterojunction displays nearly double intensity photo-response compared with pure BiOI, indicating the separation rate of photogenerated electrons and holes are improved dramatically in Ba-B-4. The free radical trapping experiments were carried out to confirm the dominant active species in photocatalysis (Fig. 1d). Potassium iodide (KI), potassium dichromate ($K_2Cr_2O_7$), tertbutylalcohol (TBA) and benzoquinone (BQ) are utilized as hole (h^+), electron (e^-), hydroxyl radical ($\bullet OH$) and superoxide radical ($\cdot O_2^-$) scavenger, respectively.³⁰ It is obvious that the photocatalytic activity is mostly restrained in adding $K_2Cr_2O_7$ scavenger, indicating the photogenerated electrons take the leading role in photocatalysis for Ba-B-4 catalyst. Thus, it can be concluded that the outstanding photocatalytic performance of the $BaCO_3$ -BiOI heterojunction should be attributed to the efficient charge separation and the photogenerated electrons are the vital factor to be considered for the enhanced photocatalysis.

3.2 Charge separation and electrons transfer

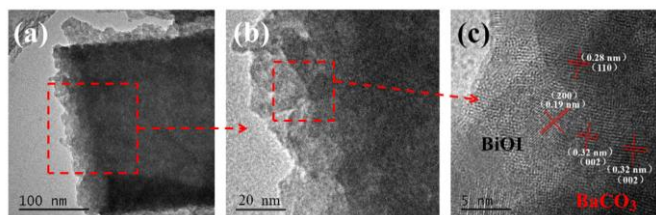


Fig. 2 TEM images (a-b) and HRTEM image (c) of Ba-B-4.

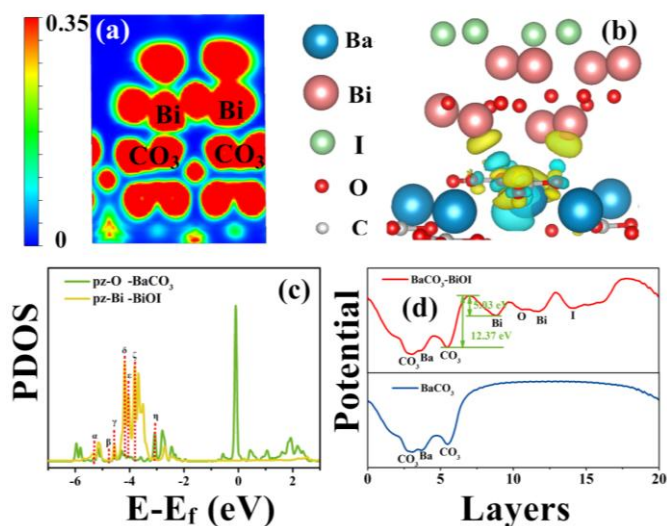


Fig. 3 (a) Electron location function (ELF); (b) Charge difference distribution between BiOI and $BaCO_3$: charge accumulation is in blue and depletion in yellow, and the isosurface is set to $0.002 \text{ eV } \text{\AA}^{-3}$; (c) Partial density of states (PDOS) of Bi atoms in BiOI and O atoms in $BaCO_3$; (d) Potential energy diagram of $BaCO_3$ -BiOI heterojunction.

atoms in $BaCO_3$: Fermi level is set to 0 eV; (d) Electrostatic potential of $BaCO_3$ -BiOI and $BaCO_3$.

To unravel the baffle of charge separation and electrons transfer in the insulator-semiconductor heterojunction, the experimental and theoretical investigations were employed and combined. The TEM images further show that the distributed BiOI nanosheets cover on the $BaCO_3$ surface (Fig. 2a-2b). The HRTEM image shows lattice spacings of 0.32 nm, 0.28 nm and 0.19 nm, which correspond to the (002) plane of $BaCO_3$ and (110) and (200) planes of BiOI, respectively (Fig. 2c). The TEM images clearly reveal that an intimate interface is formed between BiOI and $BaCO_3$, which is conducive to the free electrons transfer from one component to another. The density functional theory (DFT) was employed to further confirm the nature of the interaction between insulator ($BaCO_3$) and semiconductor (BiOI). The electron localization function (ELF) implies that the covalent bond is formed between the Bi atoms of BiOI and the carbonates of $BaCO_3$ (Fig. 3a).

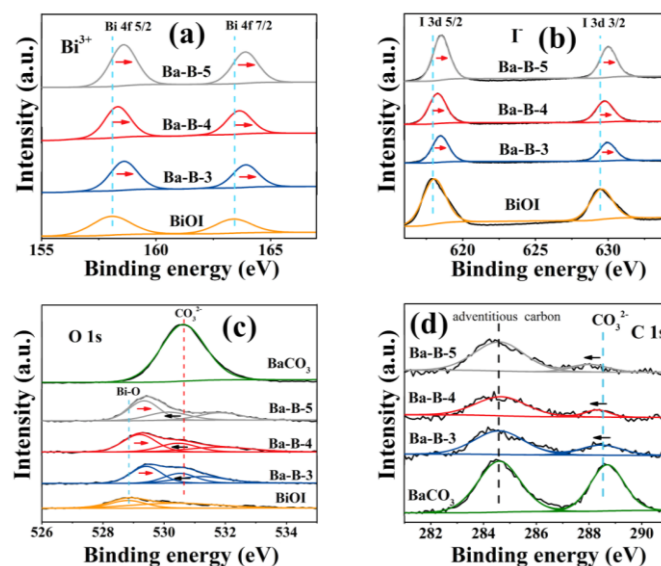


Fig. 4 XPS spectra of Bi 4f (a), I 3d (b), O 1s (c) and C 1s (d) for the samples.

The partial density of states (PDOS) is calculated (Fig. 3c), which indicate that the covalent interaction is resulted from the partial overlap of the Bi 6p and O 2p orbitals (named α , β , γ , δ , ϵ , ζ and η) in BiOI and $BaCO_3$, respectively. This enables the formation of an electronic channel for electrons transfer between the $BaCO_3$ and BiOI.^{31,32} Apart from this observation, the electrons delivery direction should be determined. The XPS spectra suggest that the binding energies for Bi 4f, I 3d and O 1s in the BiOI of Ba-B-4 are shifted to higher values compared to those in pure BiOI, whereas the binding energies for O 1s and C 1s in the $BaCO_3$ of Ba-B-4 are shifted to a lower value in comparison with pure $BaCO_3$ (Fig. 4). These chemical shifts demonstrate that the electrons transfer from BiOI to carbonate of $BaCO_3$ in the heterojunctions.³³

The charge difference distribution of $BaCO_3$ -BiOI heterojunction was calculated as shown in Fig. 3b. It can be observed that the Bi atoms of BiOI contribute to the charge depletion. The charge from Bi atoms are donated and accumulated on O atoms of $BaCO_3$.

Obviously, the electrons transfer direction is from Bi atoms of BiOI to the O atoms of BaCO₃, corresponding to the formed electrons delivery channel. In order to explore why the excited electrons of Bi could transfer to the O atoms of BaCO₃, the potentials of BaCO₃-BiOI and BaCO₃ were calculated. As shown in Fig. 3d, the potential of Bi layer (5.03 eV) is higher than that of the carbonate layer (12.37 eV) by 7.34 eV. Hence, this potential difference would drive the excited electrons from Bi atoms transfer cross the energy barrier to the adjacent carbonate layer under the visible light irradiation.

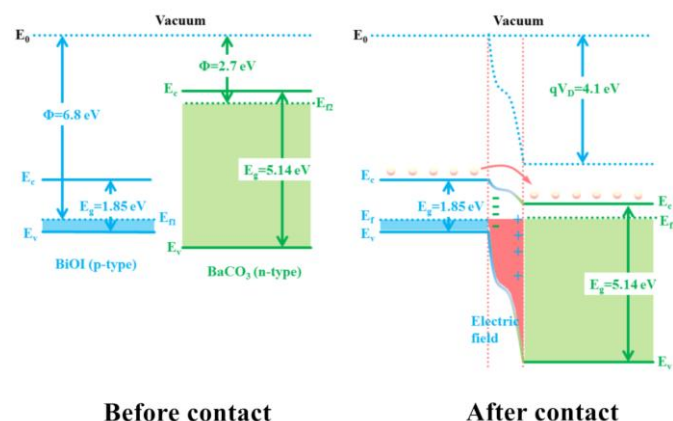


Fig. 5 Schematic diagram of band configuration and the charge separation at the interface of BaCO₃/BiOI heterojunctions under visible light irradiation; Φ is the work function, V_0 is the contact potential, E_0 is the vacuum level, E_c is the bottom of the conduction band, E_v is the top of the valence band, E_g is the band gap, E_{f1} and E_{f2} are the Fermi levels of BiOI and BaCO₃, E_f is the Fermi level of BaCO₃/BiOI heterojunctions.

In another aspect, on the basis of the work function of BiOI and BaCO₃ calculated by the Fermi level relative to the vacuum energy level, as shown in Fig. S7.³⁴ The fermi level of BiOI is lower than that of BaCO₃ (Fig. 5). When p-BiOI contacts with n-BaCO₃ to form a p-n junction (Fig. S8), the two phases will reach an equalized fermi level. And a built-in electric field directed from n-BaCO₃ to p-BiOI is established.^{13, 29} Meanwhile, the energy band of BaCO₃ will shift downward by 4.1 eV along with its fermi level in this process. The conduction band minimum (CBM) of BiOI becomes higher than that of BaCO₃ in the heterojunction, as shown in Fig. 5. Consequently, the photogenerated electrons would easily migrate from CB of BiOI to the CB of BaCO₃, leaving the holes on the VB of BiOI. Moreover, the built-in electric field could further facilitate the separation of the electron-hole pairs, making the electrons generated within BiOI move across the interface to the region of BaCO₃. Accordingly, the lifetime of photogenerated electrons should be prolonged compared with pure BiOI, which is indicated by nanosecond-level time-resolved fluorescence decay spectroscopy (Fig. S9). The radiative lifetime of Ba-B-4 is prolonged to 0.69 ns compared with that of pure BiOI (0.64 ns), which is conducive to generate more charge carriers in photocatalysis and thus boosts the efficiency of pollutants purification.

3.3 The role of separated charge carriers and photocatalytic reaction mechanism

To understand how the separated charge carriers works in photocatalysis on the insulator-semiconductor heterojunction, the electron spin resonance (ESR) spin-trap technique was employed to detect active species under visible light irradiation and the *in situ* FT-IR spectroscopy was carried out to monitor the evolution of intermediates during the photocatalytic NO purification process.

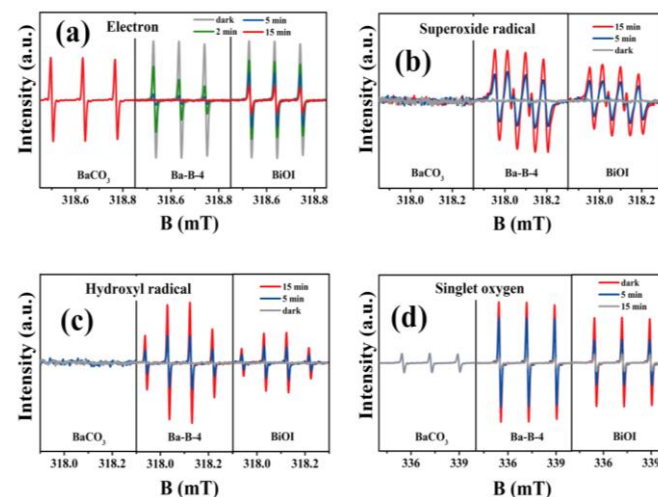


Fig. 6 DMPO ESR spin-trapping for electrons (a), superoxide radical (b), hydroxyl radical (c) and singlet oxygen (d).

As shown in Fig. 6a, the electron sacrificial agent is rapidly depleted in Ba-B-4 under light irradiation, but that of BiOI is still residual and that of BaCO₃ is not consumed at all. This result illustrates that more free electrons exist in the insulator-semiconductor heterojunction as the photogenerated electrons could transfer from BiOI to BaCO₃ and prevent the recombination of charge carriers in BiOI. Fig. 6b shows the strong superoxide radical ($\bullet\text{O}_2^-$) signals in the Ba-B-4, which is produced from that oxygen reduced by free electrons ($\text{O}_2 + \text{e}^- \rightarrow \bullet\text{O}_2^-$). BaCO₃ does not produce $\bullet\text{O}_2^-$ as it can be not excited by visible light. Significantly, the $\bullet\text{O}_2^-$ signals of Ba-B-4 is much higher than that of pure BiOI because of the electrons transfer from BiOI to BaCO₃. More holes are left in the BiOI when photogenerated electrons transfer to the BaCO₃. Hence, the signals of hydroxyl radicals ($\bullet\text{OH}$) ($\text{OH}^- + \text{h}^+ \rightarrow \bullet\text{OH}$) and singlet oxygen ($^1\text{O}_2$) ($\bullet\text{O}_2^- + \text{h}^+ \rightarrow ^1\text{O}_2$) are both stronger than that of pure BiOI (Fig. 6c-6d).³⁵ Considering the oxidation potential of the three radicals ($\bullet\text{O}_2^-$, O_2 , $\bullet\text{OH}$), the $\bullet\text{OH}$ with highest oxidation potential (3.06 V) should contribute most in the NO oxidation.

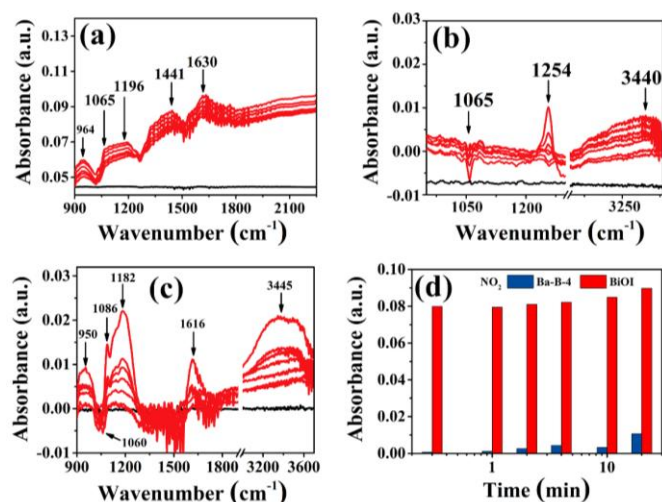


Fig. 7 *In situ* IR spectra of NO adsorption processes over BiOI (a), BaCO₃ (b) and Ba-B-4 (c) and the relative absorbance of NO₂ over BiOI and Ba-B-4 (d). (The curves follow the change of time: base-line, 20 s, 60 s, 2 min, 4 min, 8 min, 10 min and 20 min.)

Fig. 7a–7c show the NO adsorption processes over BiOI, BaCO₃ and Ba-B-4, respectively. After NO and O₂ are introduced onto the photocatalyst surface, a number of adsorption peaks appear (Table S1). On the surface of BiOI, the absorption bands of N₂O₃ (964 cm⁻¹), N₂O₂²⁻ (1065–1196 cm⁻¹), NO₂ (1441 cm⁻¹) and N₂O₂ (1630 cm⁻¹) are detected and the intensity of them is gradually increased over time, indicating the accumulation of NO adsorption species (Fig. 7a). As for BaCO₃, it was reported that NO could replace carbonates of BaCO₃, resulting in the formation of nitrites.^{36, 37} Hence, the IR bands of carbonates in BaCO₃ (1065 cm⁻¹) is decreased after NO is chemically adsorbed on the BaCO₃ surface and nitrites (1254 cm⁻¹) are simultaneously formed. The peak of N₂O is also observed at 3440 cm⁻¹ (Fig. 7b). In the case of Ba-B-4, the assignment of adsorption peaks on BiOI and BaCO₃ are all detected, such as N₂O₃ (950 cm⁻¹), free carbonate (1060 cm⁻¹), N₂O₂²⁻ (1086 and 1182 cm⁻¹), NO₂ (1616 cm⁻¹), and N₂O (3445 cm⁻¹), except for the peak of nitrites which may be overlapped by strong peak of N₂O₂²⁻ (Fig. 7c). This certifies that insulator-semiconductor heterojunction could maintain similar NO adsorption ability of BiOI and BaCO₃. Apart from that, Ba-B-4 possesses a mesoporous structure and holds larger specific surface areas (55.67 m²/g) compared with pure BiOI (10.26 m²/g) and BaCO₃ (4.98 m²/g), which are beneficial for the adsorption of contaminants and diffusion of final products (Fig. S10 and Table S2). It is noteworthy that the production of NO₂ becomes much lower over the Ba-B-4 than that on the pure BiOI surface, as shown in Fig. 7d, demonstrating the heterojunction may prevent the NO convert to the NO₂ and thus reduce the release of potential toxic intermediates.

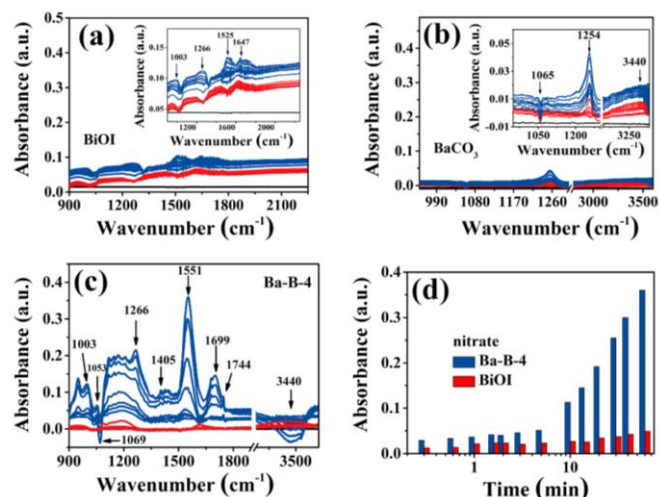


Fig. 8 The monitoring of photocatalytic NO oxidation process with *in situ* FT-IR: the adsorption curves are in red and the reaction curves are in blue over BiOI (a), BaCO₃ (b) and Ba-B-4 (c) and the relative absorbance of nitrate over BiOI and Ba-B-4 (d). (The blue curves follow the change of time: 20 s, 60 s, 2 min, 5 min, 10 min, 20 min, 40 min and 60 min.)

After reaching the adsorption equilibrium, the time-dependent IR spectra for photocatalytic reaction with BiOI, BaCO₃ and Ba-B-4 are recorded dynamically under visible-light irradiation. The photocatalytic NO oxidation process over BiOI and BaCO₃ is shown in Fig. 8a and 8b, respectively. The tendency of absorption bands under visible light irradiation is similar to that in the NO adsorption process for both of them, excepting that several weak peaks of nitrates (1003, 1266 and 1525 cm⁻¹) is detected on the surface of BiOI. In general, the photocatalytic reaction takes place very slowly. This illustrates that the separate BiOI or BaCO₃ have almost no photocatalytic capability to oxidize NO adsorption species to nitrates. Conversely, in the case of Ba-B-4, the adsorption bands of NO₂ (1616 cm⁻¹) and N₂O (3440 cm⁻¹) disappear in a short time and the adsorption peaks of the final products (nitrates) are rapidly increased over time under visible light irradiation (Table S3). **These final products accumulated on the heterojunction surface can be easily removed by water washing and the heterojunction can be regenerated via this facile method.** This implies that the photocatalytic reaction is efficient in Ba-B-4. Furthermore, two new absorption bands of NO⁺ and NO₂⁺ are observed, which are proven to be the reaction intermediates of photocatalytic NO oxidation (NO_x + radicals → NO⁺/NO₂⁺).^{38–40} Hence, their production is associated with the presence of more active species in the insulator-semiconductor heterojunction. These intermediates with high valence state could be transformed to nitrates more easily compared with other nitrogen-containing species.^{41, 42} Fig. 8d displays that the relative content of the produced nitrate in Ba-B-4 is much higher than that in pure BiOI, which arises from the constructed insulator-semiconductor heterojunction facilitating the activation of NO to form the intermediate (NO⁺ and NO₂⁺) via efficient separation and transportation of photogenerated carriers inducing abundant active species.^{41, 43} Hence, based on the results from various characterizations and theoretical calculations, the

photocatalytic mechanism of NO degradation over insulator-semiconductor heterojunction is proposed as shown in Equation (1-6) and is illustrated in Fig. 9 (Note: NO_x represents adsorption species: NO, N₂O, N₂O₂²⁻, NO₂ and N₂O₃. The radicals include ·OH, ·O₂⁻ and ¹O₂). The visible light induced electrons transfer from semiconductor BiOI to insulator BaCO₃ plays a dominant role in initiating the photocatalytic reaction and achieving efficient photocatalytic activity on this unique heterojunction.

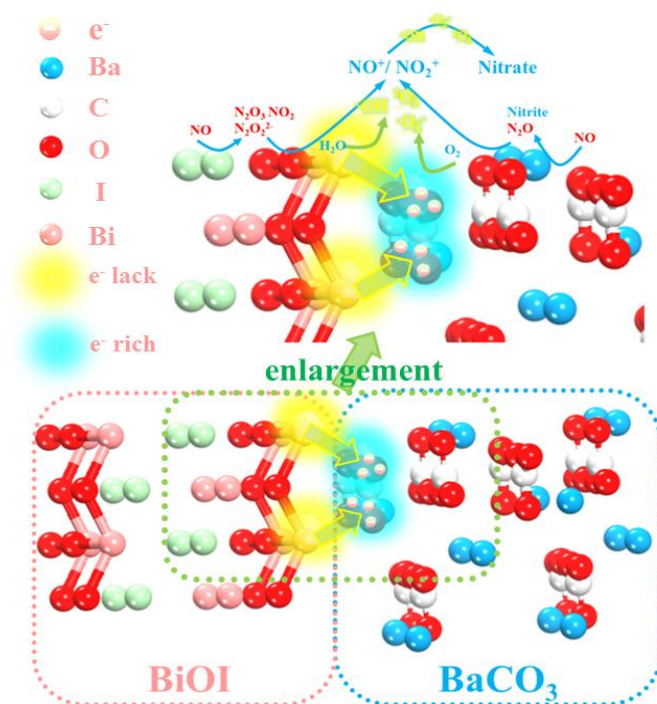
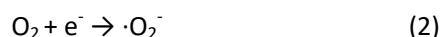
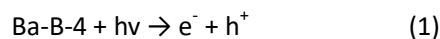


Fig. 9 Proposed schematic diagram for the separation and transfer of photogenerated carriers and photocatalytic process over insulator-semiconductor heterojunction.

4. Conclusion

Highly efficient electrons transfer from semiconductor to insulator has been achieved on BaCO₃/BiOI insulator-semiconductor heterojunctions, which enable their outstanding photocatalytic NO oxidation performance under visible light irradiation. Combining experimental and theoretical approaches, we have unraveled that an electron delivery channel is preformed in the interface between

insulator and semiconductor in the heterojunction. The potential of Bi layer of BiOI is higher than that of carbonate layer of BaCO₃, which could drive photogenerated electrons overcome the energy barrier and thus dictating the enhanced charge carrier separation. These electrons on BaCO₃ can be utilized to produce the active radicals (·OH, ·O₂⁻ and ¹O₂) participating in the photocatalytic oxidation reaction. The *In situ* FTIR spectra are used to reveal the photocatalytic promotion mechanism and corresponding conversion pathway of photocatalytic NO oxidation over insulator-semiconductor heterojunction. The active species could react with NO, making it being firstly oxidized to high valence state intermediates (NO⁺ and NO₂⁺) and then converted to the final product of nitrates. This research provides new strategy for charge carriers separation via constructing insulator-semiconductor heterojunctions and sheds atomic level insight into gas-phase photocatalytic reaction mechanism.

Acknowledgements

This work was supported by the National Natural Science Foundation of China (21777011, 21501016 and 51478070), the National Key R&D Plan (2016YFC02047), the Innovative Research Team of Chongqing (CXTDG201602014), the Key Natural Science Foundation of Chongqing (cstc2017jcyjBX0052) and the Plan for "National Youth Talents" of the Organization Department of the Central Committee. The authors also acknowledge the AM-HPC in Suzhou, China for computational support.

References

1. Y. Ma, X. Wang, Y. Jia, X. Chen, H. Han and C. Li, *Chem. Rev.*, 2014, 114, 9987-10043.
2. H. Wang, W. Zhang, X. Li, J. Li, W. Cen, Q. Li and F. Dong, *Appl. Catal. B-Environ.*, 2018, 225, 218-227.
3. W. Xing, G. Chen, C. Li, Z. Han, Y. Hu and Q. Meng, *Nanoscale*, 2018, 10, 5239-5245.
4. Z. Peng, T. Wang, X. X. Chang and J. L. Gong, *Acc. Chem. Res.*, 2016, 49, 911-921.
5. L. M. Sun, L. Xiang, X. Zhao, C. J. Jia, J. Yang, Z. Jin, X. F. Cheng and W. L. Fan, *ACS. Catal.*, 2015, 5, 3540-3551.
6. S. Luo, J. Xu, Z. Li, C. Liu, J. Chen, X. Min, M. Fang and Z. Huang, *Nanoscale*, 2017, 9, 15484-15493.
7. S. Patnaik, G. Swain and K. M. Parida, *Nanoscale*, 2018, 10, 5950-5964.
8. T. Xiong, W. L. Cen, Y. X. Zhang and F. Dong, *ACS. Catal.*, 2016, 6, 2462-2472.
9. X. Chang, T. Wang, P. Zhang, J. Zhang, A. Li and J. Gong, *J. Am. Chem. Soc.*, 2015, 137, 8356-8359.
10. K. Wenderich and G. Mul, *Chem. Rev.*, 2016, 116, 14587-14619.
11. Y. Wang, Q. Wang, X. Zhan, F. Wang, M. Safdar and J. He, *Nanoscale*, 2013, 5, 8326-8339.
12. X. Dong, W. Zhang, Y. Sun, J. Li, W. Cen, Z. Cui, H. Huang and F. Dong, *J. Catal.*, 2018, 357, 41-50.
13. H. L. Wang, L. S. Zhang, Z. G. Chen, J. Q. Hu, S. J. Li, Z. H. Wang, J. S. Liu and X. C. Wang, *Chem. Soc. Rev.*, 2014, 43, 5234-5244.
14. K. Sekizawa, S. Sato, T. Arai and T. Morikawa, *ACS. Catal.*, 2018,

- 8, 1405-1416.
15. S. Schiavoni, F. D'Alessandro, F. Bianchi and F. Asdrubali, *Renew. Sust. Energ. Rev.*, 2016, 62, 988-1011.
16. S. Lv, P. Li, J. Sheng and W. D. Sun, *Mater. Lett.*, 2007, 61, 4250-4254.
17. Z. S. Wang, M. Yanagida, K. Sayama and H. Sugihara, *Chem. Mater.*, 2006, 18, 2912-2916.
18. J. Maier, *Nat. Mater.*, 2005, 4, 805-815.
19. G. Kresse and J. Furthmüller, *Phys. Rev. B*, 1996, 54, 11169-11186.
20. G. Kresse and J. Furthmüller, *Comp. Mater. Sci.*, 1996, 6, 15-50.
21. J. P. Perdew, K. Burke and M. Ernzerhof, *Phys. Rev. Lett.*, 1996, 77, 3865-3868.
22. P. E. Blöchl, *Phys. Rev. B*, 1994, 50, 17953-17979.
23. G. Kresse and D. Joubert, *Phys. Rev. B*, 1999, 59, 1758-1775.
24. S. K. Bhatia and A. L. Myers, *Langmuir*, 2006, 22, 1688-1700.
25. R. C. Lochan and M. Headgordon, *Phys. Chem. Chem. Phys.*, 2006, 8, 1357-1370.
26. X. Feng, W. D. Zhang, Y. J. Sun, H. W. Huang and F. Dong, *Environ. Sci-Nano*, 2017, 4, 604-612.
27. F. Marias, S. Letellier, P. Cezac and J. P. Serin, *Ind. Eng. Chem. Res.*, 2014, 53, 2318-2330.
28. F. Dong, Y. H. Li, W. K. Ho, H. D. Zhang, M. Fu and Z. B. Wu, *Chinese. Sci. Bull.*, 2014, 59, 688-698.
29. H. W. Huang, Y. He, X. Du, P. K. Chu and Y. H. Zhang, *Acs. Sustain. Chem. Eng.*, 2015, 3, 3262-3273.
30. F. Dong, Z. Zhao, Y. Sun, Y. Zhang, S. Yan and Z. Wu, *Environ. Sci. Technol.*, 2015, 49, 12432-12440.
31. J. Y. Li, W. Cui, Y. J. Sun, Y. H. Chu, W. L. Cen and F. Dong, *J. Mater. Chem. A*, 2017, 5, 9358-9364.
32. J. Y. Li, X. A. Dong, Y. J. Sun, W. L. Cen and F. Dong, *Appl. Catal. B-Environ.*, 2018, 226, 269-277.
33. J. J. Liu, S. H. Zou, L. P. Xiao and J. Fan, *Catal. Sci. Technol.*, 2014, 4, 441-446.
34. P. Li, X. Zhao, C. J. Jia, H. Sun, L. Sun, X. Cheng, L. Liu and W. Fan, *J. Mater. Chem. A*, 2013, 1, 3421-3429.
35. Y. Nosaka and A. Y. Nosaka, *Chem. Rev.*, 2017, 117, 11302-11336.
36. K. Nakamoto and K. Nakamoto, *Theory & Applications in Inorganic Chemistry*, 1986, p, 88-97.
37. C. Sedlmair, K. Seshan, A. Jentys and J. A. Lercher, *J. Catal.*, 2003, 214, 308-316.
38. J. C. S. Wu and Y. T. Cheng, *J. Catal.*, 2001, 237, 393-404.
39. M. Kantcheva, *J. Catal.*, 2001, 204, 479-494.
40. K. Hadjiivanov and H. Knözinger, *Phys. Chem. Chem. Phys.*, 2000, 2, 2803-2806.
41. W. Cui, J. Y. Li, W. L. Cen, Y. J. Sun, S. C. Lee and F. Dong, *J. Catal.*, 2017, 352, 351-360.
42. L. Zhong, Y. Yu, W. Cai, X. Geng and Q. Zhong, *Phys. Chem. Chem. Phys.*, 2015, 17, 15036-15045.
43. H. Wang, W. He, X. Dong, H. Wang and F. Dong, *Sci. Bull.*, 2018, 63, 117-125.